Optics Letters

Harmonically decoupled gradient light interference microscopy (HD-GLIM)

Yi Wang,[1,2] Mikhail E. Kandel,[1,3] Michael J. Fanous,[1,4] Chenfei Hu,[1,3] HsuanYu Chen,[3] Xiaoxu Lu,[2] and Gabriel Popescu[1,3,4,*]

[1]Quantitative Light Imaging Laboratory, Beckman Institute for Advanced Science and Technology, University of Illinois at Urbana-Champaign, Urbana, Illinois 61801, USA
[2]Guangdong Provincial Key Laboratory of Nanophotonic Functional Materials and Devices, South China Normal University, Guangzhou 510006, China
[3]Department of Electrical and Computer Engineering, University of Illinois at Urbana-Champaign, Urbana, Illinois 61801, USA
[4]Department of Bioengineering, University of Illinois at Urbana-Champaign, Urbana, Illinois 61801, USA
*Corresponding author: gpopescu@illinois.edu

Received 4 October 2019; revised 29 January 2020; accepted 1 February 2020; posted 3 February 2020 (Doc. ID 379732); published 11 March 2020

Differential phase sensitive methods, such as Nomarski microscopy, play an important role in quantitative phase imaging due to their compatibility with partially coherent illumination and excellent optical sectioning ability. In this Letter, we propose a new system, to the best of our knowledge, to retrieve differential phase information from transparent samples. It is based on a 4f optical system with an amplitude-type spatial light modulator (SLM), which removes the need for traditional differential interference contrast (DIC) optics and specialized phase-only SLMs. We demonstrate the principle of harmonically decoupled gradient light interference microscopy using standard samples, as well as static and dynamic biospecimens.

https://doi.org/10.1364/OL.379732

In optical microscopy, the phase structure of transparent specimens contains important information about morphology and dynamics. However, the phase map cannot be directly observed by using ordinary bright field microscopy [1]. In the past, phase sensitive methods [2–12] have been developed to overcome this difficulty by encoding the phase information into intensity. In order to quantitatively retrieve the phase from intensity measurement, there are two main approaches: phase shifting and off-axis interferometry [13]. The former provides high space-bandwidth product at the expense of time-bandwidth product while the latter provides the reverse benefit.

The two quantitative phase imaging (QPI)-specific figures of merit, crucial for biomedical applications, are the temporal and spatial phase sensitivity. These quantities define the smallest phase shift detectable in time or space, respectively. In other words, they are the temporal standard deviation at a point in the field of view, or the spatial standard deviation within a field of view at a moment in time. It has been demonstrated that the highest temporal sensitivity is achieved by common-path techniques [14–18], which offer long-term intrinsic stability. Spatial phase sensitivity is fundamentally limited by speckles and, thus, is best using light of limited spatiotemporal coherence [16,19,20].

The differential contrast interference works well with high illumination NA. Based on this advantage, QPI applications have been recently extended to thick, multiple scattering specimens, such as embryos [17]. This approach, referred to as gradient light interference microscopy (GLIM), is capable of suppressing multiple scattering due to the high NA of the illumination, the phase shifting that subtracts the multiple scattering background, and the balanced power of the two interfering beams [21,22]. The key advantage of GLIM is the effective combination of traditional differential interference contrast (DIC) microscopy and a phase-type SLM. For accurate optical pathlength shifts in increments of $\lambda/4$ and real-time GLIM output, such SLMs are the most expensive on the market.

Other quantitative differential phase imaging technologies [3,23–28] have been reported in the past, some involving SLMs, [27,28] However, these methods are all using phase-type SLMs.

Here we present a new approach for achieving GLIM-type performance, by using a common amplitude-based SLM. This harmonically decoupled gradient light interference microscopy (HD-GLIM) setup is shown in Fig. 1. An inverted microscope (Nikon Eclipse T_i, in our case) is used to generate at the camera port a bright field image. The white light generated by a halogen lamp has a mean wavelength of $\lambda_0 = 554$ nm. The minimum and maximum illumination numerical aperture available is 0.09 and 0.55, respectively. After the field at the image plane is Fourier transformed by L_1 to the back-focal plane, an amplitude-type SLM is used to modulate the optical field. We use a sinusoidal amplitude pattern on the SLM, which splits the optical beam into three parts: +1, −1, and 0 orders, such that the field passing through the SLM:

$$\begin{aligned} U'(\boldsymbol{k}_\perp) &= U(\boldsymbol{k}_\perp)[1 + c\cos(\boldsymbol{k}_\perp \cdot \boldsymbol{x}_0 + \delta)] \\ &= U(\boldsymbol{k}_\perp) + cU(\boldsymbol{k}_\perp)\exp i(\boldsymbol{k}_\perp \cdot \boldsymbol{x}_0 + \delta) \\ &+ cU(\boldsymbol{k}_\perp)\exp[-i(\boldsymbol{k}_\perp \cdot \boldsymbol{x}_0 + \delta)]. \end{aligned} \quad (1)$$

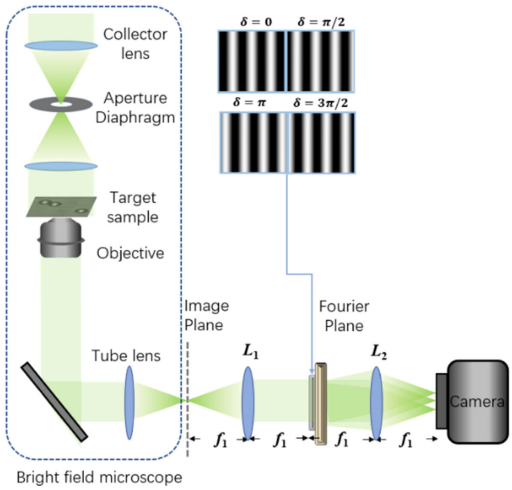

Fig. 1. Schematic demonstration of HD-GLIM system. Four phase-shifted patterns with $\Delta\delta = \pi/2$ are added on the SLM.

In Eq. (1), $U(\boldsymbol{k}_\perp)$ is the Fourier transform of the image field as a function of transverse spatial frequency $\boldsymbol{k}_\perp$, $\boldsymbol{x}_0$ is a vector that defines the spatial modulation imposed by the SLM, δ is the phase shift of the grid, which is controllable via the SLM, and c is the modulation contrast.

The period of the cosine can be expressed in the spatial domain, by noting that

$$k_\perp = \beta_0 \frac{r_\perp}{f}, \tag{2}$$

where $\beta_0 = 2\pi/\lambda_0$ is the average wavenumber in vacuum, λ_0 is the central wavelength, f is the focal distance of lens L_1, and $r_\perp$ is the spatial coordinate at the SLM plane. By adjusting x_0, one can adjust the period of the grid. Taking the inverse Fourier transform of the field in Eq. (1), we obtain the complex field at the image plane:

$$\begin{aligned} U'(r_\perp) &= U(r_\perp) + cU(r_\perp - x_0)\exp(-i\delta) \\ &\quad + cU(r_\perp + x_0)\exp(i\delta) \\ &= |U(r_\perp)|\, e^{i\phi(r_\perp)} + c\,|U(r_\perp - x_0)|\, e^{i[\phi(r_\perp - x_0) - \delta]} \\ &\quad + c\,|U(r_\perp + x_0)|\, e^{i[\phi(r_\perp + x_0) + \delta]}, \end{aligned} \tag{3}$$

where $\phi(\boldsymbol{r}_\perp)$ denotes the phase of each of the three orders. For simplicity, we used the same symbol for a function and its Fourier transform [for example, $U(\boldsymbol{k}_\perp)$ is the Fourier transform of $U(\boldsymbol{r}_\perp)$]. As a result, the measurable irradiance at the image plane is

$$\begin{aligned} I'(\boldsymbol{r}_\perp) &= \left|U'(\boldsymbol{r}_\perp)\right|^2 \\ &\simeq |U(\boldsymbol{r}_\perp)|^2 + c^2|U(\boldsymbol{r}_\perp - \boldsymbol{x}_0)|^2 + c^2|U(\boldsymbol{r}_\perp + \boldsymbol{x}_0)|^2 \\ &\quad + 4c|U(\boldsymbol{r}_\perp)|^2 \cos\left[\Delta\phi_x(\boldsymbol{r}_\perp) + \delta\right] \\ &\quad + 2c^2|U(\boldsymbol{r}_\perp)|^2 \cos\left[2\Delta\phi_x(\boldsymbol{r}_\perp) + 2\delta\right]. \end{aligned} \tag{4}$$

In Eq. (4), the approximation sign refers to $|U(\boldsymbol{r}_\perp \pm \mathbf{x_0})| \simeq |U(\boldsymbol{r}_\perp)|$, meaning that the amplitude of the field is assumed to be uniform over the distance of the shift. This is a reasonable approximation for transparent samples and a shift of the order of the point spread function or less. This is the typical approximation used in traditional DIC. The SLM provides a tunable offset δ in increments of $\pi/2$. The quantity $\Delta\phi_x(\boldsymbol{r}_\perp)$ is the phase shift of interest, defined as

$$\begin{aligned} \Delta\phi_x(\boldsymbol{r}_\perp) &= \phi(\boldsymbol{r}_\perp) - \phi(\boldsymbol{r}_\perp - \boldsymbol{x}_0) \\ &= \phi(\boldsymbol{r}_\perp + \boldsymbol{x}_0) - \phi(\boldsymbol{r}_\perp) \\ &\simeq \mathbf{x_0} \cdot \nabla_x \phi(\boldsymbol{r}_\perp). \end{aligned} \tag{5}$$

In Eq. (5), we used the fact that for a small spatial shift $\boldsymbol{x}_0$, $\Delta\phi(\boldsymbol{r}_\perp)$ is proportional to the phase gradient at that point. Thus, $\delta = n\pi/2$, $n = 0, 1, 2, 3$, the combination of the respective intensities, In, allows us to retrieve $\Delta\phi(\boldsymbol{r}_\perp)$ as

$$I_1(\boldsymbol{r}_\perp) - I_3(\boldsymbol{r}_\perp) = 8c|U(\boldsymbol{r}_\perp)|^2 \cos\Delta\phi_x(\boldsymbol{r}_\perp), \tag{6a}$$

$$I_2(\boldsymbol{r}_\perp) - I_4(\boldsymbol{r}_\perp) = 8c|U(\boldsymbol{r}_\perp)|^2 \sin\Delta\phi_x(\boldsymbol{r}_\perp), \tag{6b}$$

$$\Delta\phi_x(\boldsymbol{r}_\perp) = \mathrm{Arg}[I_1(\boldsymbol{r}_\perp) - I_3(\boldsymbol{r}_\perp),\ I_2(\boldsymbol{r}_\perp) - I_4(\boldsymbol{r}_\perp)]. \tag{6c}$$

Equations (6a)–(6c) indicate that the second-harmonic interference terms can be decoupled from the measured intensities, and $\Delta\phi_x(\boldsymbol{r}_\perp)$ can be obtained uniquely. Once $\Delta\phi_x(\boldsymbol{r}_\perp)$ is obtained, we can integrate it into $\phi(\boldsymbol{r}_\perp)$ along the x direction, since the spatial shift $\boldsymbol{x}_0$ is known. According to previous works [3,29], it is known that the differential phase information along both x and y directions, combined with the spiral integration algorithm, is more robust than integrating a single component of the phase gradient. Thus, modulating the SLM in the perpendicular direction, in addition to $\Delta\phi_x(\boldsymbol{r}_\perp)$, we also measure $\Delta\phi_y(\boldsymbol{r}_\perp)$, following the same procedure. In order to measure the exact spatial shift, $\boldsymbol{x}_0$, we compare the simulated phase of the 4.5 μm microbead with the experimentally measured one. Given that the refractive index of the immersion oil we used is 1.518 and that of microbeads 1.546 at 25 μm and central wavelength $\lambda_0 = 554.3$ nm, the expected phase of a 4.5 μm microbead is simulated by using $\phi(\boldsymbol{r}_\perp) = (2\pi/\lambda_0)h(\boldsymbol{r}_\perp)\Delta n$. As illustrated in Fig. 2, by fitting the experimental and simulated data, we find that the actual spatial shift of our system is $x_0 = 524$ nm under a 40× magnification objective. Next, to quantitatively assess the spatiotemporal noise level of our HD-GLIM system, we acquired a time lapse movie of a $30 * 30\ \mu m^2$

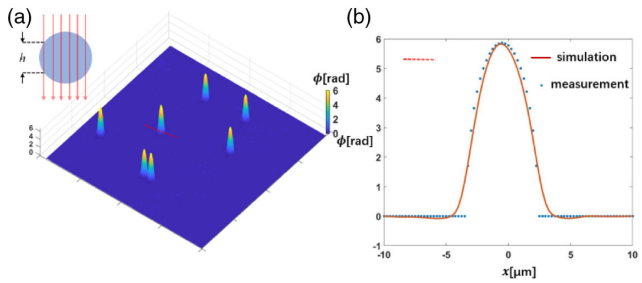

Fig. 2. (a) Phase distribution of 4.5 μm polymetric microbeads. (b) Simulation and measurement data.

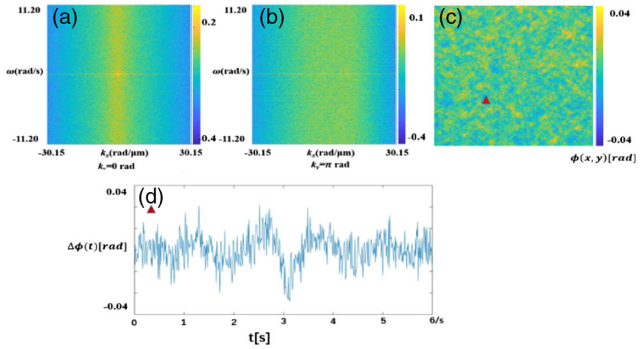

Fig. 3. (a) and (b) Spatiotemporal noise distribution with log operation at $k_x = 0$ and $k_x = \pi$. (c) Spatial noise distribution. (d) Temporal phase fluctuation of the point marked in (c). Color bar in (a) and (b) is $rad^2/[rad/\mu m]^2[rad/s]$.

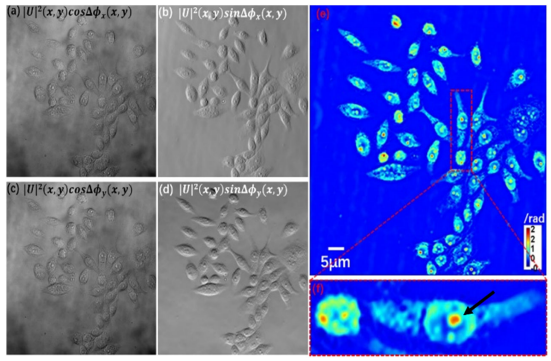

Fig. 4. (a)–(d) Four differential interference data used for phase demodulation. (e)–(f) Phase of CW620 cells and its corresponding details.

field of view without a sample, over 6 s, at 40 frames per second, which is shown in Visualization 1. We take the spatiotemporal power spectrum of these data, $P(k_x, k_y, \omega)$, and normalize the total noise variance, σ^2.

In Figs. 3(a) and 3(b), the noise distribution section of two different spatial frequencies is shown. We further characterize the spatiotemporal phase noise using the histogram shown in Fig. 3(e), with the standard deviation as indicated.

We used the HD-GLIM to perform QPI of both the cell and tissue samples. SW620 cells were allowed to grow in a culture dish for 72 h before fixation.

Then the sample was washed twice with the phosphate-buffered saline (PBS) buffer before it was covered with 1.5 ml of 4% paraformaldehyde solution for 15 min at room temperature. The fixed sample was then washed with PBS buffer three times; then it was kept in 2 ml PBS. Images were acquired within 48 h post-fixation. An illustration of imaging SW630 cells with HD-GLIM is shown in Fig. 4. Both the interferometric intensity and the phase data are shown, as indicated. We can see apparent DIC features in Figs. 4(a)–4(d). The resulting integrated phase map is shown in Fig. 4(e), with a zoomed-in area shown in Fig. 4(f). The arrow points to the nucleolus of a cell, of the order of a micron in diameter. These results indicate that the HD-GLIM system can be used to obtain high-resolution phase information from cells. One of the posited uses of quantitative imaging is to address observational bias in clinical setting [30].

HD-GLIM can address this challenge by being sufficiently sensitive to capture thin, histologically prepared specimen, such as the H&E stained pancreas tissue, having hyalinized islets of Langerhans, shown in Fig. 5. Figures 5(a)–5(d) show the four differential interference images of a field of view of the hyalinized pancreatic section. Figures 5(b)–5(d) and Fig. 5(b)–5(d) bear typical gradient DIC features. Figures 5(e)–5(g) are zoomed-in images of the constructed phase map [Fig. 5(f)], which consists of cells near the base of a pancreatic acinus. These results indicate that the HD-GLIM system can be used successfully to produce high-quality phase information from various biological specimens.

In this Letter, we extended the microscope control software used to support the acquisition of a variable number of frames. Exposing the camera for 30 ms and allowing the modulator to stabilize for 150 ms. To perform imaging, we use a real-time, simplified, version of the phase retrieval algorithm that operates along one dimension of the image. With the help of our software, we used the HD-GLIM system for dynamic measurements of live cells. QPI has been proven to be a powerful tool for investigations in neuron science [31].

In Visualization 1, we measure the dynamic phase evolution of a neuron cell over a period of 1 h. In this video, we can observe the dynamics of cell structures, which indicates that HD-GLIM provides the necessary phase stability for cell dynamics measurement.

Furthermore, once we fully open the condenser, we can achieve an excellent optical section effect using the HD-GLIM system. First, we suspend the 4.5 μm microbeads and let them locate at different focus planes of our system. We show the phase results at the 0 and 20 μm in Fig. 6. We can apparently see that the out-of-focus information has been suppressed well in HD-GLIM system according to these results.

In summary, we developed a new system to perform QPI. This system does not rely on the traditional DIC optics, which is likely to allow for easier adoption for biological studies. Using an amplitude SLM to modulate spatially the image field and applying controlled phase shifts, we capture several intensity images, decoupled and eliminated the harmonic term, and retrieved the pure phase information. We calculate the exact spatial shift by fitting the simulation and experimental data of the proposed system and calibrate it to the most satisfactory level. Then we quantified the phase sensitivity of the system by using spectral analysis and a spatiotemporal histogram method.

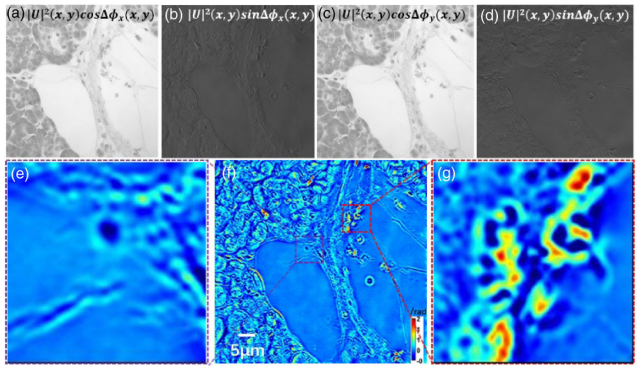

Fig. 5. (a)–(d) Four differential interference data used for phase demodulation. (e)–(g) Phase of pancreas tissue and its different details.

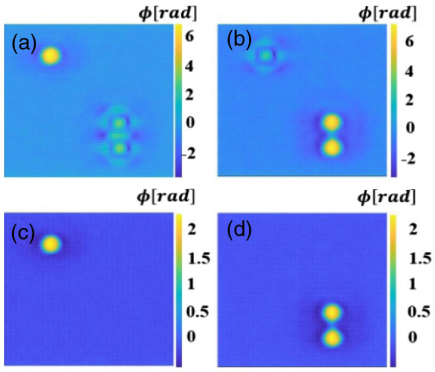

Fig. 6. (a) and (b) Phase results under NAc = 0.09. (c) and (d) are the phase results under NAc = 0.55.

Using the proposed system, we measure both static and dynamic biological samples to show its performance. At last, we experimentally demonstrated the excellent optical sectioning effect of the proposed system under high NA illumination.

Funding. National Institute of General Medical Sciences (GM129709); National Cancer Institute (CA238191); National Science Foundation (2013AA014402, CBET0939511 STC, NRT-UtB 173525).

Disclosures. The authors declare no conflicts of interest.

REFERENCES

1. G. Popescu, *Quantitative Phase Imaging of Cells and Tissues* (McGraw-Hill, 2011).
2. P. Marquet, B. Rappaz, P. J. Magistretti, E. Cuche, Y. Emery, T. Colomb, and C. Depeursinge, Opt. Lett. **30**, 468 (2005).
3. M. R. Arnison, K. G. Larkin, C. J. Sheppard, N. I. Smith, and C. J. Cogswell, J. Microsc. **214**, 7 (2004).
4. H. Ding, Z. Wang, F. Nguyen, S. A. Boppart, and G. Popescu, Phys. Rev. Lett. **101**, 238102 (2008).
5. F. Merola, P. Memmolo, L. Miccio, R. Savoia, M. Mugnano, A. Fontana, G. D'Ippolito, A. Sardo, A. Iolascon, and A. Gambale, Light Sci. Appl. **6**, e16241 (2017).
6. Y. Cotte, F. Toy, P. Jourdain, N. Pavillon, D. Boss, P. Magistretti, P. Marquet, and C. Depeursinge, Nat. Photonics **7**, 113 (2013).
7. H. V. Pham, C. Edwards, L. L. Goddard, and G. Popescu, Appl. Opt. **52**, A97 (2013).
8. M. Mir, H. Ding, Z. Wang, K. Tangella, and G. Popescu, J. Biomed. Opt. **15**, 027016 (2010).
9. H. Majeed, S. Sridharan, M. Mir, L. Ma, E. Min, W. Jung, and G. Popescu, J. Biophoton. **10**, 177 (2017).
10. H. Pham, B. Bhaduri, H. Ding, and G. Popescu, Opt. Lett. **37**, 3438 (2012).
11. C. Edwards, B. Bhaduri, T. Nguyen, B. G. Griffin, H. Pham, T. Kim, G. Popescu, and L. L. Goddard, Opt. Express **22**, 5133 (2014).
12. A. Greenbaum, W. Luo, T.-W. Su, Z. Göröcs, L. Xue, S. O. Isikman, A. F. Coskun, O. Mudanyali, and A. Ozcan, Nat. Methods **9**, 889 (2012).
13. Y. Park, C. Depeursinge, and G. Popescu, Nat. Photonics **12**, 578 (2018).
14. B. Bhaduri, C. Edwards, H. Pham, R. Zhou, T. H. Nguyen, L. L. Goddard, and G. Popescu, Adv. Opt. Photon. **6**, 57 (2014).
15. Z. Wang, L. Millet, M. Mir, H. Ding, S. Unarunotai, J. Rogers, M. U. Gillette, and G. Popescu, Opt. Express **19**, 1016 (2011).
16. B. Bhaduri, H. Pham, M. Mir, and G. Popescu, Opt. Lett. **37**, 1094 (2012).
17. T. H. Nguyen, M. E. Kandel, M. Rubessa, M. B. Wheeler, and G. Popescu, Nat. Commun. **8**, 210 (2017).
18. G. Popescu, L. L. Goddard, P. S. Carney, T. Kim, R. Zhou, M. A. Mir, and S. D. Babacan, "White light diffraction tomography of unlabeled live cells," U.S. patent 9,404,857 (2 August 2016).
19. Y. Choi, T. D. Yang, K. J. Lee, and W. Choi, Opt. Lett. **36**, 2465 (2011).
20. H. Ding and G. Popescu, Opt. Express **18**, 1569 (2010).
21. J. M. McCracken, B. M. Rauzan, J. C. Kjellman, M. E. Kandel, Y. H. Liu, A. Badea, L. A. Miller, S. A. Rogers, G. Popescu, and R. G. Nuzzo, Adv. Healthcare Mater. **8**, 1800788 (2019).
22. Z. Yan, M. Han, Y. Shi, A. Badea, Y. Yang, A. Kulkarni, E. Hanson, M. E. Kandel, X. Wen, and F. Zhang, Proc. Natl. Acad. Sci. USA **114**, E9455 (2017).
23. P. Bon, G. Maucort, B. Wattellier, and S. Monneret, Opt. Express **17**, 13080 (2009).
24. D. Fu, S. Oh, W. Choi, T. Yamauchi, A. Dorn, Z. Yaqoob, R. R. Dasari, and M. S. Feld, Opt. Lett. **35**, 2370 (2010).
25. A. Nativ, H. Feldman, and N. T. Shaked, Appl. Opt. **57**, 3534 (2018).
26. H. Schreiber and J. Schwider, Appl. Opt. **36**, 5321 (1997).
27. T. J. McIntyre, C. Maurer, S. Fassl, S. Khan, S. Bernet, and M. Ritsch-Marte, Opt. Express **18**, 14063 (2010).
28. T. J. McIntyre, C. Maurer, S. Bernet, and M. Ritsch-Marte, Opt. Lett. **34**, 2988 (2009).
29. S. Bernet, A. Jesacher, S. Fürhapter, C. Maurer, and M. Ritsch-Marte, Opt. Express **14**, 3792 (2006).
30. M. E. Kandel, S. Sridharan, J. Liang, Z. Luo, K. Han, V. Macias, A. Shah, R. Patel, K. Tangella, and A. Kajdacsy-Balla, J. Biomed. Opt. **22**, 066016 (2017).
31. C. Hu and G. Popescu, IEEE J. Sel. Top. Quantum Electron. **25**, 8458413 (2019).